

Cryogenic setup for trapped ion quantum computing

M.F. Brandl,^{1, a)} M.W. van Mourik,¹ L. Postler,¹ A. Nolf,¹ K. Lakhmankiy,¹ R.R. Paiva,^{1,2} S. Möller,³ N. Daniilidis,³ H. Häffner,³ V. Kaushal,⁴ T. Ruster,⁴ C. Warschburger,⁴ H. Kaufmann,⁴ U.G. Poschinger,⁴ F. Schmidt-Kaler,⁴ P. Schindler,¹ T. Monz,¹ and R. Blatt^{1,5}

¹⁾*Institut für Experimentalphysik, Universität Innsbruck, Technikerstraße 25, A-6020 Innsbruck, Austria*

²⁾*São Carlos' Physics Institute, University of São Paulo, Av. Trabalhador São-Carlense, 400, São Carlos, SP, Brazil*

³⁾*Dept. of Physics, University of California, Berkeley, CA 94720, USA*

⁴⁾*QUANTUM, Institut für Physik, Universität Mainz, Staudingerweg 7, 55128 Mainz, Germany*

⁵⁾*Institut für Quantenoptik und Quanteninformation der Österreichischen Akademie der Wissenschaften, Technikerstraße 21a, A-6020 Innsbruck, Austria*

(Dated: 19 July 2016)

We report on the design of a cryogenic setup for trapped ion quantum computing containing a segmented surface electrode trap. The heat shield of our cryostat is designed to attenuate alternating magnetic field noise, resulting in 120 dB reduction of 50 Hz noise along the magnetic field axis. We combine this efficient magnetic shielding with high optical access required for single ion addressing as well as for efficient state detection by placing two lenses each with numerical aperture 0.23 inside the inner heat shield. The cryostat design incorporates vibration isolation to avoid decoherence of optical qubits due to the motion of the cryostat. We measure vibrations of the cryostat of less than ± 20 nm over 2 s. In addition to the cryogenic apparatus, we describe the setup required for an operation with $^{40}\text{Ca}^+$ and $^{88}\text{Sr}^+$ ions. The instability of the laser manipulating the optical qubits in $^{40}\text{Ca}^+$ is characterized yielding a minimum of its Allan deviation of $2.4 \cdot 10^{-15}$ at 0.33 s. To evaluate the performance of the apparatus, we trapped $^{40}\text{Ca}^+$ ions, obtaining a heating rate of 2.14(16) phonons/s and a Gaussian decay of the Ramsey contrast with a 1/e-time of 18.2(8) ms.

PACS numbers: 03.67.Lx, 07.20.Mc, 37.10.Ty

I. INTRODUCTION

The applications of trapped ions in Paul traps range from mass-spectrometry¹ and frequency standards^{2,3} to quantum simulation⁴ and quantum computation (QC) where they enable architectures which are promising candidates for fault-tolerant QC^{5,6}. There, linear segmented Paul traps provide the means to reconfigure the ion crystals where the quantum operations are applied onto varying subsets of ions⁷.

Here, we describe an experimental setup containing a cryostat as the cryogenic temperatures solve the following challenges towards large-scale QC with trapped ions. (i) Performing the necessary ion string reconfiguration operations requires micro-fabricated traps which yield ion-to-electrode distances between 50 and 200 μm . This vicinity of the ions to the electrode surfaces results in a higher susceptibility to electric field noise which disturbs the quantum operations⁸. It has been observed that these detrimental effects are suppressed in traps that are operated at cryogenic temperatures^{9,10}. (ii) With increasing numbers of ions in the traps^{11,12}, collisions with background gas cause ion loss, making large scale QC impossible. Operating the trap in a cryogenic environment offers access to vacuum pressures not accessible in

room temperature setups. A conservative upper bound for vacuum pressures reached in cryostats is 10^{-15} mbar at a temperature of 4 K which is about 4 orders of magnitude lower than typical vacuum pressures in room temperature vacuum chambers¹³. (iii) When ions are used as a quantum memory, magnetic field fluctuations are the main source of decoherence¹⁴. This can be mitigated in a cryostat, as a copper heat shield at cryogenic temperatures can be used to suppress alternating magnetic fields¹⁵.

Operating an ion trap in a cryostat adds additional design challenges as the operation of any type of cryostat causes vibrations in the vacuum chamber. These vibrations have to be decoupled from the ion trap, while maintaining a good thermal contact, as coherent manipulation of optical qubits requires localization of the ions below the corresponding wavelength for the time of manipulation.

Furthermore, large-scale QC with trapped ions will involve ion crystal reconfiguration which will induce kinetic energy into the system¹⁶. To remove this energy, sympathetic cooling with multiple ion species^{17,18} is employed in our setup. We focus on the operation with $^{40}\text{Ca}^+$ and $^{88}\text{Sr}^+$ ions and their respective optical qubits¹⁹ and describe the required laser system and control electronics.

In Section II, we describe our cryogenic setup and focus especially on vibrations, magnetic shielding against alternating magnetic fields, and the trap. The laser setup required for our trapped ion QC experiments is described

^{a)}Electronic mail: Matthias.Brandl@uibk.ac.at

in Section III. Section IV covers the electronic setup used in our experiments, and finally we present results of first characterization measurements with trapped ions in Section V.

II. THE CRYOGENIC SETUP

When designing a cryogenic system, the first considerations address the type of cryostat. For our setup, we considered closed cycle cryostats, like Gifford-McMahon and Pulse Tube cryocoolers, which do not require a supply of liquid coolant, and wet cryostats, like bath cryostats and (continuous) flow cryostats, which require a supply of liquid coolant but do not require additional electrical power. Wet cryostats do not produce acoustic noise, other than closed cycle cryostats. Such noise in the lab will cause vibrations in all parts of the experiment. When working with optical qubits¹⁹ in a trapped ion QC setup, the experiments will be sensitive to the phase of the light at the position of the ion. Therefore, vibrations on the order of the wavelength of visible light reduce the coherence of an optical qubit. It is, thus, beneficial to work with a wet cryostat which additionally allows tuning the temperature of the cold finger as well. Hence, we decided to work with a flow cryostat²⁰.

Two heat shields, shown in Figure 1, are used to reduce the coolant consumption. The evaporated coolant from the inner stage cools the outer stage. Since the outer heat shield completely surrounds the inner heat shield, it will reduce the black-body-radiation induced heat load on the inner shield. Additionally, the heat load is further decreased by polishing and silver-plating all parts of the cryostat.

A. Mechanical stability and vibrations

Peak-to-peak vibrations due to the operation of a flow cryostat are usually on the order of $1 \mu\text{m}$ at the tip of the cold finger.²¹ In order to suppress this movement, vibrational decoupling between the cold finger and the ion trap is required. The incorporated decoupling scheme²² contains a membrane bellow which reduces the mechanical coupling between the cold finger and the vacuum chamber, as depicted in Fig. 1. The inner shield, containing the ion trap, is mounted through rigid mounts with low thermal conductivity to the outer shield and the vacuum chamber. At cryogenic temperatures, the cold finger and the heat shields are connected through thin oxygen-free high conducting (OFHC) copper wires, see Fig. 1, to reduce the transmitted vibrations while retaining excellent thermal conductivity. Varying the number of wires enables finding a trade-off between vibrations and thermal contact.

The mount structure connecting the outer shield to the vacuum chamber is a hexapod made of 316LN stainless steel, as illustrated in Fig. 2. Hexapods provide high

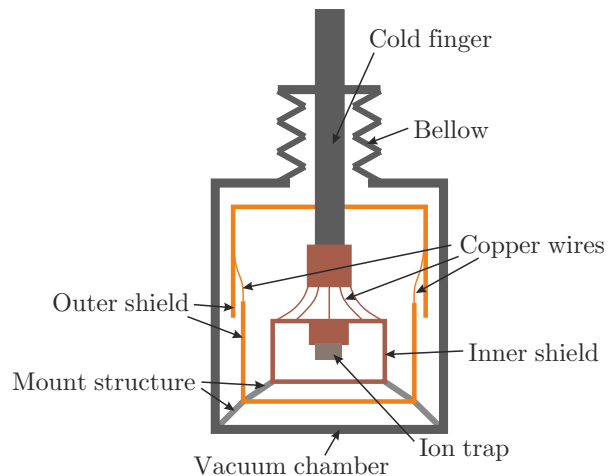


FIG. 1. Schematic of the vibrational decoupling. The inner shield, which contains the ion trap, is rigidly mounted to the vacuum chamber through mounts and the outer heat shield. The cold finger is connected via a bellow to the vacuum chamber and can vibrate independently of the vacuum chamber. The heat contact between the cold finger and the other heat shield is provided through thin copper wires.

stability at a small cross-section, thus combining high rigidity with low thermal conductance. Due to space constraints, a stainless steel cylinder with a very thin wall ($\approx 0.5 \text{ mm}$) connects the inner and the outer shield. This mount has a higher mechanical stability but also a higher thermal conductivity than a hexapod with the same cross-section. During operation with liquid helium, this is the largest contribution to the heat load of the inner heat shield, but still below 200 mW.

The whole vacuum chamber is illustrated as cutaway view in Figure 3. In addition to the vibration isolation in the vacuum vessel, aluminum cross bars were installed outside the vacuum chamber to prevent movement of the vacuum chamber with respect to the optical table on which it is mounted.

The mount structure shown in Fig. 2 is designed to withstand force in the vertical direction, because it has to support about 23 kg of weight of the copper shields. The hexapod extends from the mount to the vacuum chamber to the mount of the outer shield. From there, the cylindrical mount connects to the lower inner shield. This mount structure resembles a double pendulum which is mechanically less rigid horizontally than vertically. Hence, we only investigated the vibrations in the horizontal plane, and assumed the vibrations in vertical direction to be much smaller than in the horizontal plane.

An interferometric distance measurement with a Michelson interferometer was employed to measure the differential length of the two interferometer arms, as depicted in Fig. 4. The two mirrors of the interferometer arms were a reference mirror on the optical table and a mirror in the inner shield. This allowed us to measure the differential movement between the optical table and

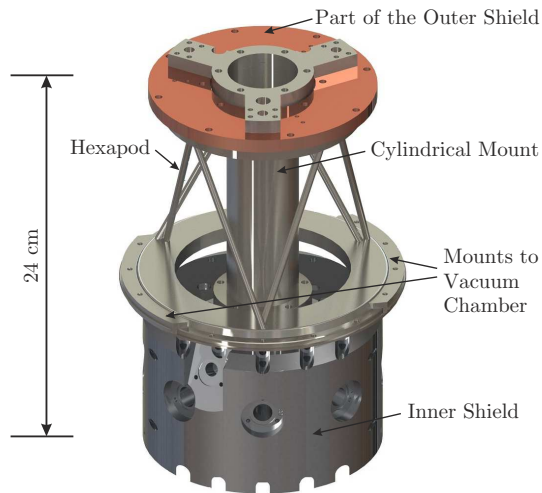


FIG. 2. Sketch of the rigid mounting structure. A hexapod connects the vacuum chamber and the outer shield, and a cylindrical mount connects the outer and the inner shield.

the inner shield. In order to measure the full movement of the inner shield, a second Michelson interferometer was placed perpendicular to the first one to record the movements in two directions at the same time.

The recorded movements are shown in Fig. 5 a. The two measurement axes were chosen along and perpendicular

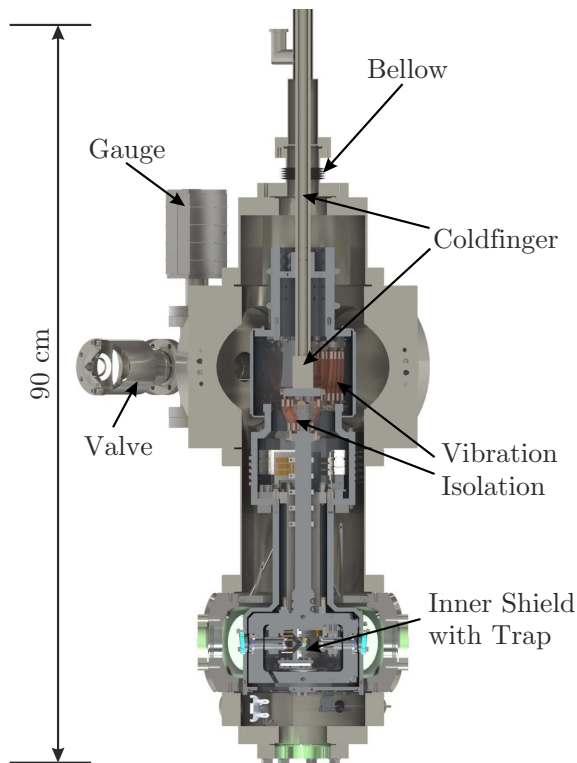


FIG. 3. A cutaway view of the cryostat.

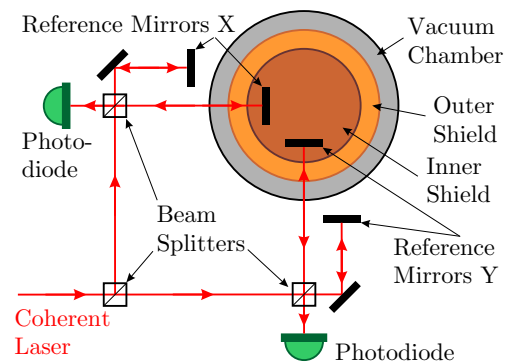


FIG. 4. Two Michelson interferometers employed to measure the vibrations in a 2D plane simultaneously.

ular to the axis of the Paul trap in the cryostat. The vibrations along both axes are on the same order of magnitude and stay between ± 20 nm over 2 s. Fig. 5 b depicts the Fourier transform of these vibrations. The peaks around 30 and 45 Hz correspond to the eigenfrequencies of the inner shield and the peaks between 90 and 100 Hz to the eigenfrequencies of the vacuum chamber. The amplitude of the movement is much smaller than the wavelength of the qubit transitions, about 700 nm, allowing for coherent manipulation of optical qubits. All measurements were performed in absence of acoustic noise in the lab. Additional noise can easily increase the vibration amplitudes by a factor of 10 or more.

Long-term measurements over 10 min show an inner shield movement of less than ± 120 nm from the original position. We attribute this movement to the vibration isolation of the optical table. Due to small residual movements of the table, the vacuum chamber on the optical table is slightly tilted which leads to the observed movements. At the current state of trapped ion QC, typical quantum algorithms²³⁻²⁵ require a processing time of about 1 ms. Further analysis showed that during 3-5 ms, the phase shifts of the qubit laser light at the position of the trap are dominated by acoustic vibrations coupling into the optical setup but not by movement of the inner shield in the vacuum chamber. Hence, our cryogenic setup promises to have the same coherence properties as room temperature setups where coherence times of tens of ms have been observed¹⁴.

B. Magnetic field shielding

Our setup is designed for operation with $^{40}\text{Ca}^+$ and $^{88}\text{Sr}^+$ ions. The available qubit transitions of these ion species have magnetic field dependences of up to $2\pi \cdot 39$ GHz/T^{19,26,27}. In order to not be limited by magnetic field fluctuations, the magnetic fields have to be stabilized both spatially and temporally so that the frequency shift due to magnetic perturbations is smaller than the natural linewidth of the qubit transition, which

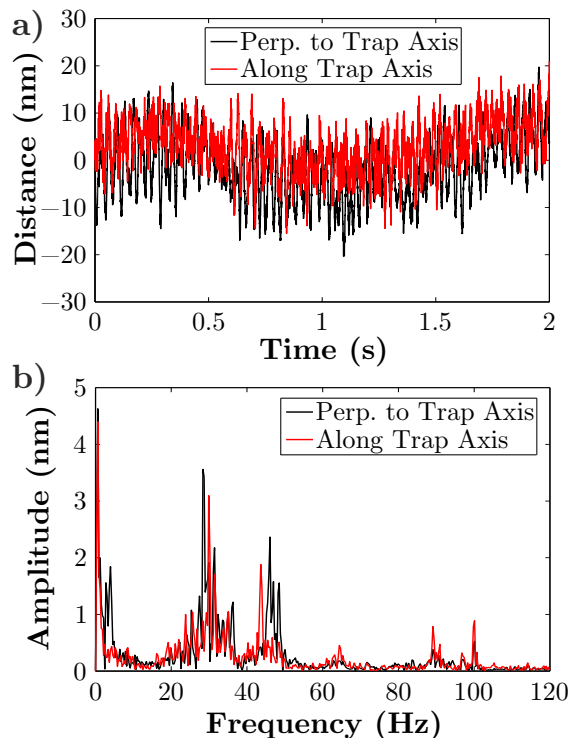


FIG. 5. The measured vibrations of the cryostat cooled with liquid nitrogen. Panel a) depicts the vibrations over time and Panel b) the Fourier-transform of these vibrations.

for both ion species is the ${}^2S_{1/2} \leftrightarrow {}^2D_{5/2}$ transition. In Ca^+ , the qubit transition has a linewidth of about 140 mHz^2 , in Sr^+ it is 400 mHz^3 . Hence, the magnetic field perturbations during one experimental cycle should not exceed $140 \text{ mHz} / (39 \text{ GHz/T}) = 3.6 \text{ pT}$. In our experiments, the typical quantization field strength is about 0.3 mT . Therefore, relative magnetic field stability better than about $1.2 \cdot 10^{-8}$ both spatially and temporally is required.

In this setup, the homogeneity is achieved by using Helmholtz coils, which have an average radius of 19.5 cm . Simulations show that this results in an inhomogeneity below the desired level of $1.2 \cdot 10^{-8}$ over a length of 1.5 mm around the trap center. Hence, it will be possible to address ion strings over this length with a global beam simultaneously. In order to achieve the desired magnetic field homogeneity, magnetic materials must not be used in the cryostat design.

Technologically, it is challenging to actively stabilize magnetic fields with the required precision over time. However, passive filtering by exploiting the skin effect of a surrounding metal is feasible, as well as the generation of constant magnetic fields with superconducting coils. Since this setup is not big enough to incorporate superconducting Helmholtz coils with a radius of 19.5 cm , our choice was to reject alternating magnetic fields with thick OFHC copper walls¹⁵. The remaining dependence

on slow drifts, e.g. set point of the current driver of the coils, or changes in earth's magnetic field, can be eliminated by interleaving actual measurements with calibration measurements²⁸.

The damping of alternating magnetic fields with OFHC copper relies on the skin effect which prevents AC magnetic fields from penetrating a conductor. The skin depth δ is given by

$$\delta = \sqrt{\frac{2}{\omega \sigma \mu}} \quad (1)$$

with ω the (angular) frequency of the magnetic field, σ the conductivity of the material, and μ its permeability. At low temperatures, the conductivity of the copper becomes so high that magnetic field at frequencies as low as a couple of Hertz are suppressed over lengths in the cm or even the mm range.

Experience has shown that the main spectral components of magnetic field fluctuations in trapped ion QC experiments are synchronous to the power line frequency. Therefore, magnetic field attenuation is most important at a frequency of 50 Hz and its harmonics. At room temperature, the skin depth of 50 Hz magnetic fields is about 9.2 mm in copper. The inner shield of our cryostat is made of ultra-pure copper that was thermally annealed in a nitrogen atmosphere at $450 \text{ }^\circ\text{C}$ to increase its conductivity at cryogenic temperatures. When cooling with liquid helium, we estimate a conductivity increase by a factor between 100 and 1000 as compared to room temperature. Therefore, the skin depth due to skin effect at 50 Hz will decrease to a value between 0.92 mm and 0.29 mm . In this setup, the walls of the inner shield are 20 mm thick such that we calculate a magnetic shielding of -188 dB or even -600 dB for 50 Hz fields. These numbers elaborate that the cold, thick copper walls are excellent magnetic shields for frequencies of 50 Hz and higher. In trapped ion experiments, the expected attenuation is lower due to holes in the shields for optical access, and physical barriers for the eddy currents repelling the magnetic field fluctuations. For the latter case, contact resistances between two parts of the shield are typically limiting the magnetic shielding.

For appropriate access to install the ion trap, its surrounding heat shield has to consist of at least two parts. Eddy currents run in circles perpendicular to the magnetic field fluctuations that cause them. Therefore, the inner shield is cut into two pieces along a plane perpendicular to the quantization magnetic field, as can be seen in Fig. 6. Along this axis (depicted by the green arrow), the sensitivity to magnetic fields is the strongest as fluctuations perpendicular to the axis have little influence on the absolute value of the magnetic field. Thus, the shield was designed to have the strongest attenuation in this direction. Eddy currents (depicted by red arrows) produced by magnetic fields along this axis run parallel to this plane and are not affected by the contact resistance between the two halves of the inner shield. Eddy

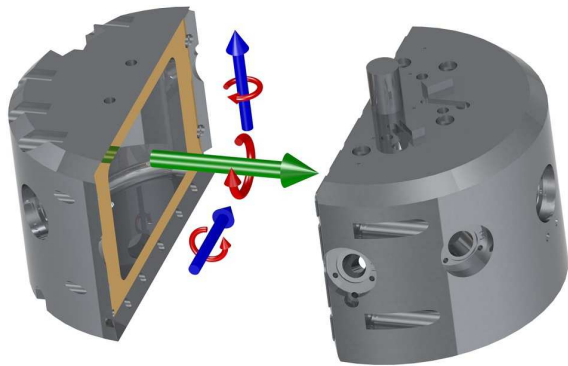


FIG. 6. Sketch of the two halves of the inner heat shield. The green arrow symbolizes the magnetic field axis, the blue arrows represent the two axis perpendicular to the magnetic field axis, and the red arrows depicted induced eddy currents and their orientation.

currents caused by magnetic field fluctuations in different directions (depicted by blue arrows in Fig. 6) have to pass from one half to the other and will be limited by the contact resistance between the two halves of the heat shield at low temperatures. Therefore, the magnetic shielding will be less efficient in directions perpendicular to the quantization axis.

In order to characterize the magnetic shield, magnetic magnetoresistive sensors²⁹ were placed inside the inner shield. We calibrated the sensitivity of the sensor for the current temperature by applying a step signal to the coils.

For the magnetic shielding measurement, a sinusoidal magnetic field of various frequencies was generated by the field coils and the response signal of the magnetic sensor was measured. Employing the calibration of the sensitivity, one obtains the attenuation for a specific frequency. The measurement results corresponding to the direction of the quantization axis can be seen in Fig. 7 for various temperatures. The measurement limit with our setup was between -60 and -55 dB and was mainly limited by pickup outside the vacuum chamber. The magnetic shielding improves with decreasing temperature. Below 20 K, the attenuation saturates, which suggests that the electrical conductivity of the used copper is constant at temperatures of 20 K and lower. This means that in order to reduce the coolant consumption, it is sufficient to operate the cryostat at a temperature of the inner shield slightly below 20 K. Lower temperatures do not reduce the vacuum pressure, as hydrogen, the main constituent element of background gas, condensates at 20 K.

Table I summarizes the measured attenuations of magnetic fields at 50 Hz and the estimated upper bounds. For temperatures below the boiling point of liquid nitrogen, the attenuation for 50 Hz magnetic fields exceeds the measurement capabilities. However, an upper bound for the attenuation can be determined. The attenuation due to skin effect along a direction x scales as $\exp(-x/\delta)$ with

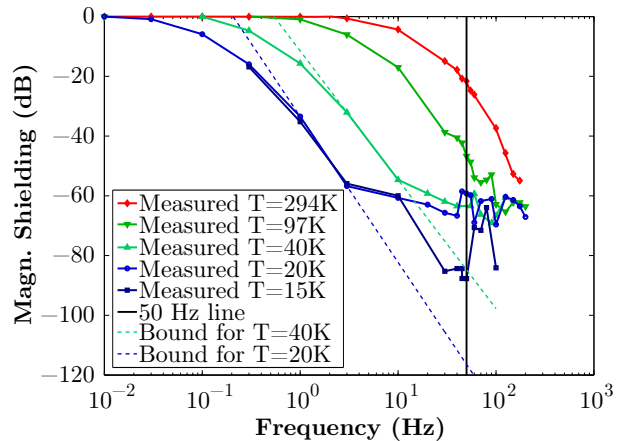


FIG. 7. The magnetic shielding over frequency along the quantization axis for various temperatures of the inner heat shield.

the skin depth δ from eq. 1. Hence, the gradient of the attenuation becomes greater with increasing frequency, if the attenuation is limited by skin-effect. Extrapolating the last two data points above this noise floor, we estimate an attenuation of 120 dB as indicated in Fig. 7.

The comparison of the magnetic shielding along the quantization axis and perpendicular to it is depicted in Fig. 8. At room temperature, the contact resistance is not the limiting factor, and there is no significant difference between the magnetic shielding along and perpendicular to this magnetic field axis. By contrast at low temperatures, the conductivity of the copper increases sharply, and the contact resistance becomes the limiting factor. Hence, the magnetic shielding perpendicular to the axis will be worse than along the axis. Since the contact resistance is not frequency dependent, magnetic shielding limited by contact resistance will have a constant gradient in a double logarithmic plot. As shown in Fig. 8, the shielding of magnetic fields of 50 Hz perpendicular to the quantization axis is about -60 dB, whereas along the axis the upper bound is -120 dB.

The measured attenuation was so high that the trapped ion qubits are decoupled from ambient alternating magnetic fields which are typically in the low μT regime in typical laboratory environments. Slow magnetic field drifts, like offset drifts of the current in the coils or changes in earth's magnetic field, will still affect the qubits in the inner shield. However, dynamical decoupling sequences³⁰ with a periodicity faster than the frequencies that can penetrate the inner shield de-

TABLE I. Table of attenuations for 50 Hz magnetic fields at various temperatures. Extrapolated values are displayed in italics.

Temperature	294 K	97 K	40 K	20 K
Attenuation	21 dB	46 dB	85 dB	<i>120 dB</i>

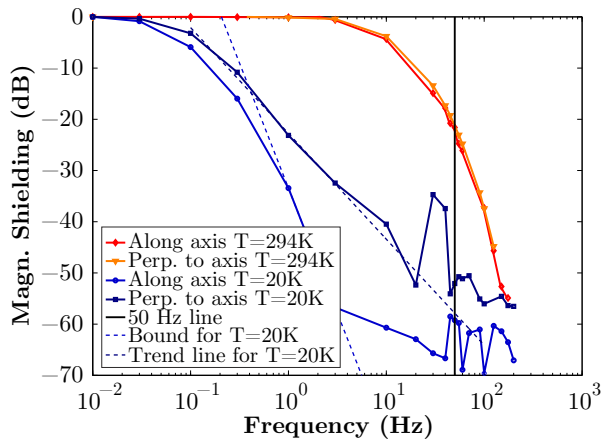


FIG. 8. The magnetic shielding along the quantization axis and perpendicular to it, when the inner heat shield is at room temperature and at 20K.

couple the experiments from these low frequency magnetic field drifts. Additional calibration measurements between quantum information experiments can be introduced to infer the qubit transition frequencies²⁸.

C. Trap and beam geometries

A universal set of quantum gates for quantum computing³¹ requires the capability to address single ions³². In order to optically address single ions with a wavelength of about 700 nm and typical axial trap frequencies of up to 1 MHz³³, a diffraction-limited addressing requires a numerical aperture (NA) of about 0.2 or higher. Following the approach of reference 5, a scalable trapped ion quantum computer will require a structured Paul trap. For ease of scalable trap fabrication, our trap is designed such that all electrodes lie in a single plane, as illustrated in Fig. 9 a. Two RF-electrodes, both 60 μm wide, provide radial confinement. The outer DC segments have a width of 200 μm separated by 10 μm wide and 30 μm deep gaps from the other electrodes. The 100 μm wide slot in the center electrode allows for light with a numerical aperture of up to 0.24 to pass through without scattering from the edges of the slot. The trap was structured by *Translume*³⁴ and gold-coated in-house by angle evaporation³⁵ to prevent electric connection through the trenches and to cover the central slit with metal.

In typical experiments with segmented ion traps, all beams are parallel to the plane of the trap. The required NA for single-ion addressing makes different beam geometries necessary. As depicted in Fig. 9 a, our trap has a slit through which all beams have to pass. The only exception is a global qubit beam, which runs parallel to the surface and addresses all ions in the trap simultaneously. The addressing qubit beam with the high NA

for single-ion addressing is perpendicular to the surface. The beams used for cooling, detection and initialization, depicted in blue, are oriented 45° to the trap surface. In order to allow state initialization with optical pumping, one of these two beams is oriented along the magnetic field axis of the experiment (σ -light). The other one is perpendicular to it (π -light).

Electrostatic simulations predict a pseudo-potential minimum of 100 μm above the trap surface, resulting in a minimal electrode-to-ion distance of 113 μm . In order to define the boundary conditions more reliably, a gold-plated clamp displayed in Fig. 9 b is placed around the trap. In addition, the central electrode is connected to an RF connection to allow for global qubit rotations between Zeeman substates using RF-fields.

If the addressing and detection optics were placed entirely outside the cryostat, the desired NA of 0.2 would require holes of large diameter in the heat shield, which would deteriorate the magnetic shielding efficiency. In order to achieve the required NA, we placed lenses close to the ion trap in the cryogenic environment, such that only collimated beams of small diameter have to pass through the heat shields. To increase the collection efficiency of scattered photons, two lenses, one at the front and one at the back of the trap, were placed inside the inner shield, as displayed in Fig. 10 a.

The used aspherical lenses with half-inch diameter³⁶ have a focal length of 25 mm and an NA of 0.23. Their custom anti-reflection-coating allows using the lenses for single ion addressing with the qubit lasers around a wavelength of 700 nm as well as for detection of fluorescence around a wavelength of 400 nm. Thermal contraction of the lens and its mount leads to mechanical stress on the lens which will cause birefringence in the lens. To circumvent this, a cylindrical mount with long slits was designed, shown in Fig. 10 b. The long slits act as flat springs to reduce mechanical stress. Because of the round shape of this mount, the remaining mechanical stress should be symmetrical, and thus not cause birefringence.

An advantage of having the lenses in the inner shield is that the addressing beams can pass through the glass of the viewport, the outer and inner shield as collimated beams. That way, aberrations deteriorating the qubit addressing capabilities are reduced. Alternatively, complicated objectives consisting of several lenses outside the vacuum would need to compensate for aberrations caused by the viewport. Typically, these are more sensitive to aberrations caused by off-center or tilted beams than a single lens. Furthermore, as the ion trap, the inner shield and the focusing lenses represent one rigid mechanical assembly, alignment errors due to small movement of the inner shield are strongly suppressed compared to external focusing optics. The only significant misalignment in the path of the addressing beam can originate in a change of the angle under which the incoming beam hits the last lens. This is caused outside of the vacuum vessel and has to be considered in the design of the addressing optics.

Using the lenses for detection, each lens collects about

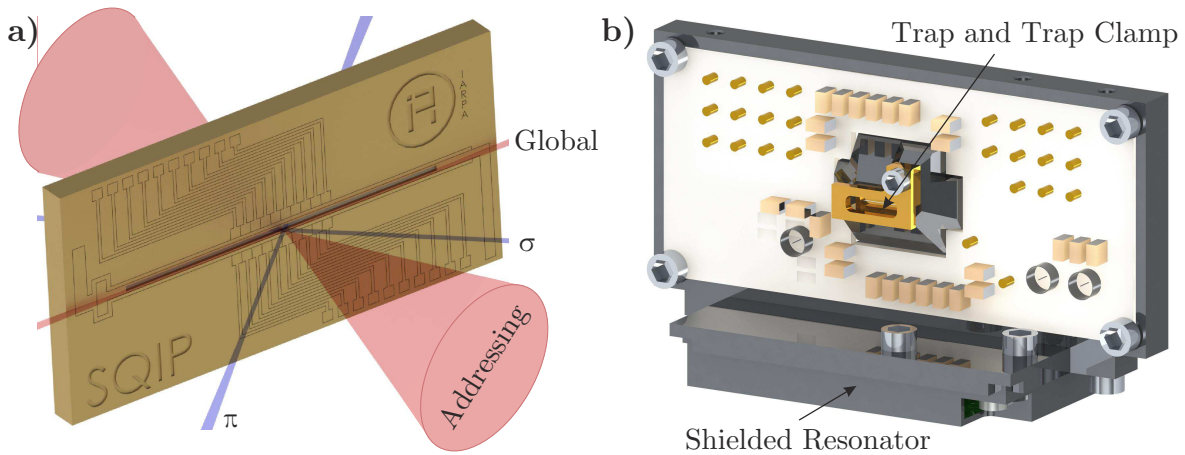


FIG. 9. Panel a) shows a sketch of our trap with the laser beams for state manipulation. Panel b) displays a the trap mounting structure with the attached shielded resonator.

1.3 % of the light emitted by the ions in the focal point of the lens. With a typical magnification of about 30, we are able to image ion strings of 50 ions onto our electron multiplying charge-coupled device (EMCCD) camera³⁷.

The resonator to generate the RF voltage in the Paul trap was a shielded RLC-series resonator. It is mounted

underneath the trap in the inner heat shield. The resonator coil is made of a high temperature superconductor with a critical temperature above 87 K. It has an inductance of $1.6 \mu\text{H}$ resulting in a resonance at 49.9 MHz. Details on the design of this resonator can be found in reference 38. With less than 100 mW of RF power, we could load ions and operate the trap.

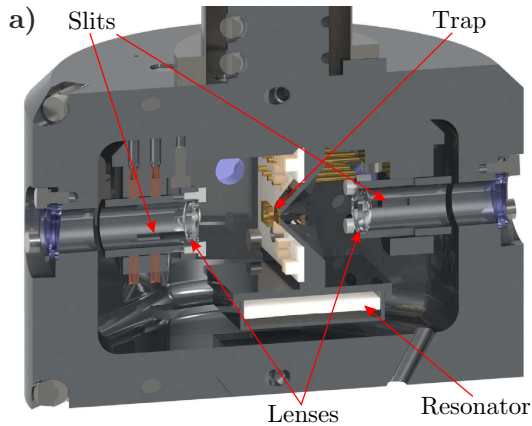


FIG. 10. Trap and optical assembly inside the inner shield. Panel a) depicts a cut through the sketch of the inner heat shield with the trap, the resonator and the lenses for addressing and detection. Panel b) shows a picture of a lens mount.

III. LASER SETUP

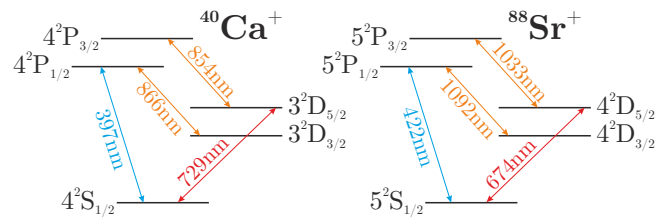


FIG. 11. Energy level diagrams for $^{40}\text{Ca}^+$ and $^{88}\text{Sr}^+$

Motional heating⁸ poses a limit on quantum information processing in large scale ion trap quantum computers, and it will require recooling of ion strings without affecting the quantum states of the qubits. A suitable technique is sympathetic cooling^{17,18}, where a second ion species is used to cool heterogeneous ion crystals. Therefore, we work with $^{40}\text{Ca}^+$ and $^{88}\text{Sr}^+$ ions. Their level structure, which can be seen in Fig. 11, is identical, while the corresponding transition wavelengths and radiative lifetimes are different. Henceforth, when we denote transitions without specifying an ion species, it means that the statement is applicable to both ion species. In our approach to trapped ion QC, read-out and quantum state manipulation are done with timed light pulses. The optical qubit is encoded in the transition $^2\text{S}_{1/2} \leftrightarrow ^2\text{D}_{5/2}$. This

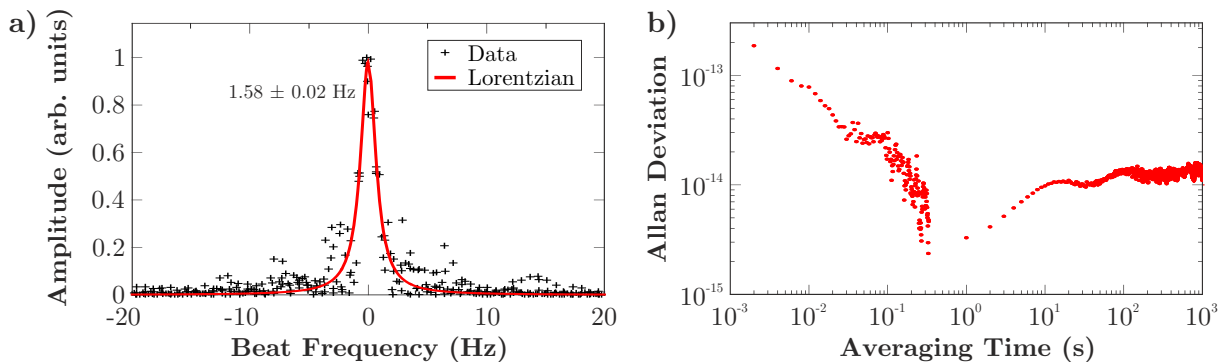


FIG. 12. Panel a) illustrates the beat note of our 729nm-laser with a second 729nm-laser. The Lorentzian fit results in a linewidth of $1.58(2)\text{Hz}$. Panel b) shows the Allan deviation over averaging time. The lowest observed Allan deviation was $2.4 \cdot 10^{-15}$ at an averaging time of 0.33 s.

is a dipole forbidden transition, and hence, ${}^2\text{D}_{5/2}$ is a metastable state with a life-time on the order of 1 s. The D-state life-time of each species is long compared to typical gate times on the order of $10 \mu\text{s}$ and allows coherent manipulation. Coherent optical driving of the transition requires a constant phase of the light, which is only ensured with a laser whose frequency is constant during the qubit manipulation. State detection is a projective quantum measurement for which we employ state-dependent resonance fluorescence. There, laser beams resonant to the transitions ${}^2\text{S}_{1/2} \leftrightarrow {}^2\text{P}_{1/2}$, and ${}^2\text{D}_{3/2} \leftrightarrow {}^2\text{P}_{1/2}$ will induce fluorescence of an ion if the outer electron is in the ${}^2\text{S}_{1/2}$ state. If the outer electron is in the ${}^2\text{D}_{5/2}$ state, the ion will stay dark. To reset the qubit, an additional laser for the transition ${}^2\text{D}_{5/2} \leftrightarrow {}^2\text{P}_{3/2}$ is employed. The exact wavelengths for these transitions can be found in references 2, 3, and 33.

In the following, we will discuss the lasers required for the operation of our experiment. To load ions into the trap, an oven is heated up until it emits a beam of neutral atoms. In this setup, there are two commercial ovens³⁹, one filled with Ca and one filled with Sr, mounted inside the vacuum chamber without thermal contact to the cryostat. These atoms are ionized by photo-ionization^{40,41}. For the isotope-sensitive laser excitation during the ionization process, external cavity diode lasers (ECDL) are used⁴². Broadband light sources with enough intensity in the required wavelength range are employed for the non-isotope-sensitive part of the ionization.

The lasers driving the dipole transitions in both ion species are ECDLs⁴³, which are frequency stabilized to reference cavities using the Pound-Drever-Hall (PDH) scheme⁴⁴. The sole exception is the 397 nm laser⁴⁵ which is a frequency-doubled laser and the light at 794 nm is locked to a cavity. The typical finesse of the reference cavities are between 500 and 1000, and the free spectral range (FSR) is 1.5 GHz. This results in typical linewidths on the order of 100 kHz for our lasers. One of the two mirrors of each cavity is mounted on piezos which allows

very precise frequency tuning. Hence, it is possible to tune each cavity to an arbitrary frequency around the corresponding dipole transition of the ion.

In our experiments, the quadrupole ${}^2\text{S}_{1/2} \leftrightarrow {}^2\text{D}_{5/2}$ transition is used as the qubit transition^{2,3,19,33}. To achieve coherence times longer than 100 ms, a linewidth of the laser driving this transition of less than 10 Hz is required. Both qubit lasers are ECDLs⁴⁶ with an extended optical resonator. The free running natural linewidth of such an ECDL can be on the order of 1 MHz. Hence, the frequency stabilization has to reduce the linewidth by five or six orders of magnitude. This is challenging with a single stage, and thus, a two-stage approach⁴⁷ was pursued for the 729nm laser and the 674nm laser.

The first stage is a PDH lock to a pre-stabilization cavity with medium finesse (MF) of about 10000, which is located on the same cavity spacer as the optical resonators for the dipole lasers, yielding a FSR of 1.5 GHz. This results in a linewidth between 1 and 10 kHz after the first locking stage.

The second stage is another PDH lock in which the feedback acts through a voltage controlled oscillator (VCO) driving an acousto-optic modulator (AOM). This feedback loop is referenced to a high-finesse (HF) cavity⁴⁸ with a finesse of about 250000 with and an FSR of 3 GHz. This light is then amplified with a tapered amplifier before it is sent to the experiment.

Since the pre-stabilization cavity contains two piezos, which have a non-zero thermal expansion (of first order), its length will thermally drift with respect to the HF cavity, making their resonance frequencies drift apart. Due to the limited bandwidth of the VCO driving the AOM, this drift is compensated with a field programmable gate array (FPGA)-based counter which feeds back on one of the piezos of the MF cavity to compensate the thermal drift.

In order to measure the linewidth of the laser, beat measurements of the 729nm laser with the laser used in reference 2 were performed. The results of these beat measurements can be seen in Fig. 12. With a finesse

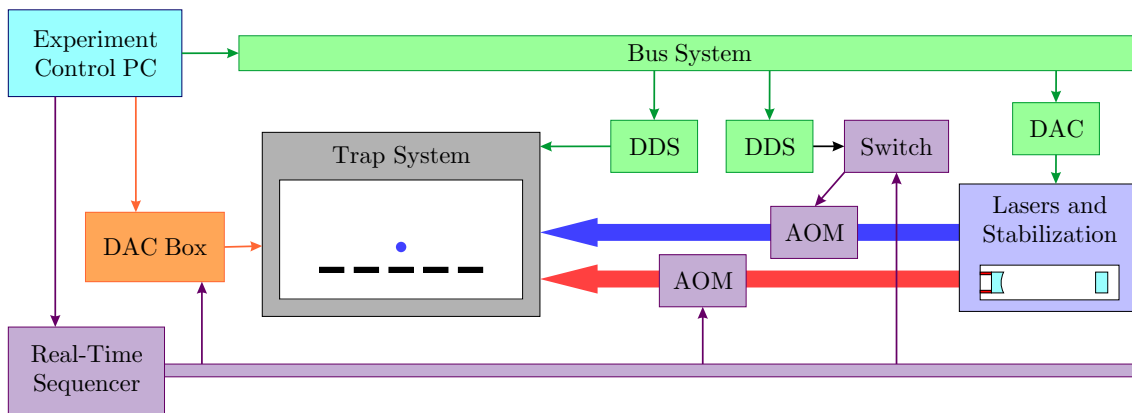


FIG. 13. The schematic of the experiment control. Before the measurement, the preset signals like the voltages to set the laser frequencies or the trap drive RF are programmed via the bus system. During the experiment, the real-time sequencer switches qubit lasers directly on and off with internal DDSs. Other laser beams are controlled via RF switches. Furthermore, the sequencer triggers the DAC box to control the trap DC voltages of the trap.

of 242742(6) of our 729nm cavity, a Lorentzian fit of the beat signal of the two 729nm lasers resulted in a linewidth of 1.58(2) Hz⁴⁹. Additionally, the Allan deviation of the beat signal was calculated and resulted in a lowest Allan deviation of $2.4 \cdot 10^{-15}$ at an averaging time of 0.33 s. We expect a similar performance from our 674nm laser as we use the same lock system for both lasers. However, due to the lack of a second 674nm laser of similar linewidth, we could not perform the same measurements with our 674nm laser.

IV. ELECTRONICS

In trapped ion QC experiments, the following signals have to be accurately controlled:

- Radio-frequency (RF) for the RF-drive of the Paul trap
- DC voltages for the cavity piezos to tune the laser frequencies
- Light has to be switched on and off with sub-microsecond precision
- Signals for phase-coherent qubit manipulation
- DC voltages to confine the ion string(s) axially

It is beneficial to distinguish between quasi-static signals and dynamical fast signals. Quasi-static signals are signals which can be set before a measurement. They include for example the amplitude and frequency of the RF voltage to drive the Paul trap or the DC voltages applied to cavity piezos to tune the laser frequencies. The dynamical fast signals have to be varied during a measurement. They contain for example the phases of RF signals required for phase-coherent manipulation of laser light.

To control the quasi-static signals, we use a digital bus system⁵⁰ developed at the University of Innsbruck, as depicted in Fig. 13. The bus has 8 address bits, 16 data bits, and 1 strobe bit, which are sent via a 50 pin ribbon cable, where every second pin is grounded. The ground lines in the ribbon cable cause a considerable capacitance, which limits the transmission length to about 5 m before the signal has to be digitally refreshed to provide a bit error probability below 10^{-8} at a bus timing of 1 μ s. The digital refreshing is performed by bus driver cards, which provide galvanic isolation between their input signals and their output signals and, thus, also prevent ground loops.

The bus system has output cards for analog voltages, digital voltages, and RF signals. These output cards allow us to generate the signal close to their targets. The RF signals are generated with direct digital synthesizer (DDS) chips, and allow setting an RF signal before a measurement sequence, which can be switched on and off via an RF switch during a sequence. The switching of an RF signal can be converted to switching of an optical signal with an AOM in single pass or double pass configuration. The output cards are mounted in rack systems, which additionally support RF amplifiers, sample-and-hold PID controllers, and other cards that are of use in the lab.

In trapped ion QC experiments, typical single qubit gate times are on the order of 1 to 10 μ s. When all quasi-static signals are set, our real-time sequencer with a timing resolution of 10 ns starts the measurement. The sequencer, depicted in Fig. 13, can control digital outputs and react to digital inputs. Furthermore, it features DDSs, which allow phase-coherent frequency switching and amplitude shaping of RF signals.

The DC voltages for confining and moving ions are supplied by an FPGA-based arbitrary waveform generator designed and built at the University of Mainz¹⁶. This arbitrary waveform generator is triggered by a digital sig-

nal from the real-time sequencer to allow movement of ions during a measurement.

V. EXPERIMENTS WITH TRAPPED IONS

Two non-evaporative getters⁵¹ in the vacuum chamber allow us to typically achieve pressures of below 10^{-8} mbar at room temperature. Then, we precool for 24 to 36 hours with liquid nitrogen to reduce the liquid helium consumption during further cool down. After switching to liquid helium, it usually takes a couple of hours to reach our typical operating temperatures of about 20 K. At these temperatures, our cryogenic system typically consumes 0.5 l liquid helium per hour. We estimate that only 50% of this consumption is due to thermal leakage in the experimental vacuum chamber. The remaining 50% of this consumption are caused by the dewar and the transfer line.

Under typical operating temperatures of about 20 K, we trap ions and obtain trap lifetimes of several hours under continuous Doppler cooling. We recorded Rabi flops on the carrier with a sideband cooled $^{40}\text{Ca}^+$ ion using the global beam, shown in Fig. 14. A measurement of the average phonon number resulted in roughly 0.1 phonons along the trap axis, whereas the observed decay corresponds to an average phonon number of 14. Therefore, we assume that the ion was radially at a temperature well above the Doppler cooling limit.

We can use an ion image on the EMCCD camera to characterize the detection optics, as shown with a $^{40}\text{Ca}^+$ ion in Fig. 15. The magnification of the imaging system is 15, and the sum over the rows and columns of the region of interest are in agreement with Gaussian fits of $1.84(7) \mu\text{m}$ width and $1.89(11) \mu\text{m}$ height.

Next, we characterized the qubit addressing capabilities³² of the $\text{NA} = 0.23$ lens. For this measurement, a $^{40}\text{Ca}^+$ ion is moved along the trap axis through the addressing beam and the Rabi flops for different positions were measured. From the Rabi frequency, the light intensity at one position along the trap axis can be

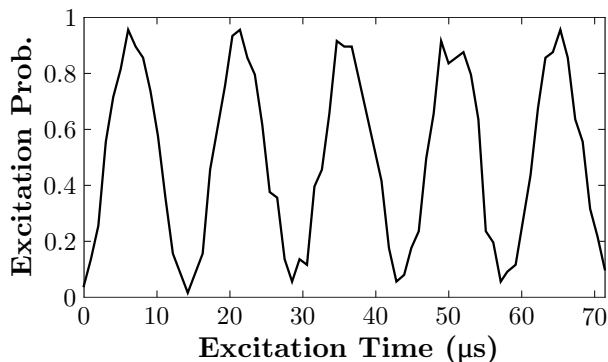


FIG. 14. Rabi flops with a sideband cooled ion.

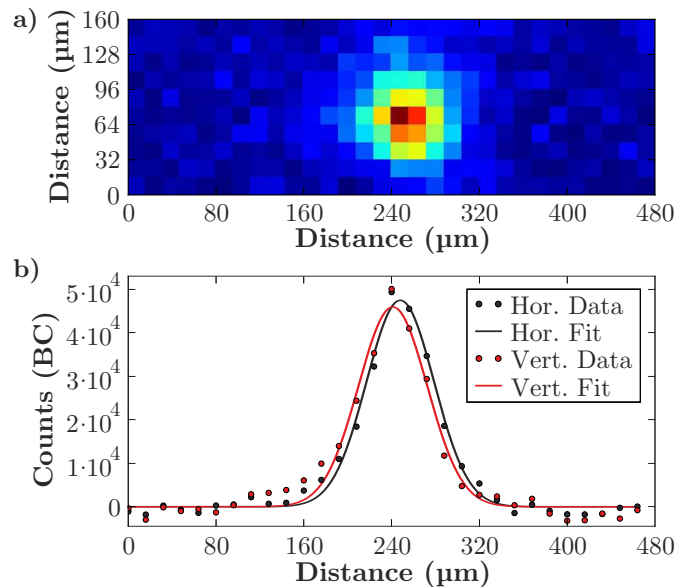


FIG. 15. Panel a) depicts an image of a $^{40}\text{Ca}^+$ ion on an EMCCD camera. Panel b) displays the averaged background corrected (BC) counts of the ion along a horizontal and vertical axis. The counts represent Gaussian fits showing few aberrations in the detection optics.

determined. The obtained intensity profile of the beam along the trap axis is depicted in Fig. 16. The measured beam waist is $3.0(1) \mu\text{m}$.

Motional coherence is required in entangling gate operations^{52,53}. The heating rate is a rate of change of motional quanta of the secular motion in phonons per second, and high motional heating rates in a trap limit the fidelity of entangling gates. Thus, the heating rate of a trap is a quantity of interest for trapped ion quantum information processing setups. The heating rate is obtained by measuring the mean phonon number after

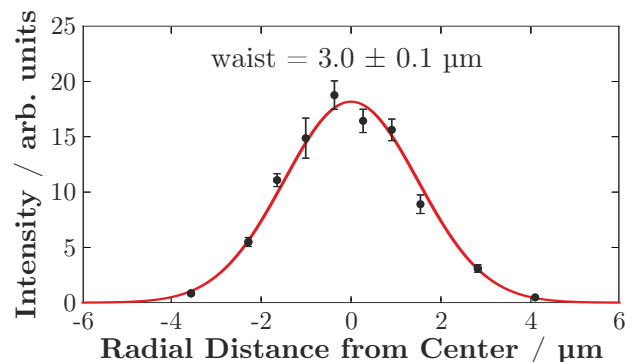


FIG. 16. Test of our addressing optics. A single ion was moved along the trap axis through the addressing beam and the measured light intensity is measured, resulting in a beam waist of $3.0(1) \mu\text{m}$.

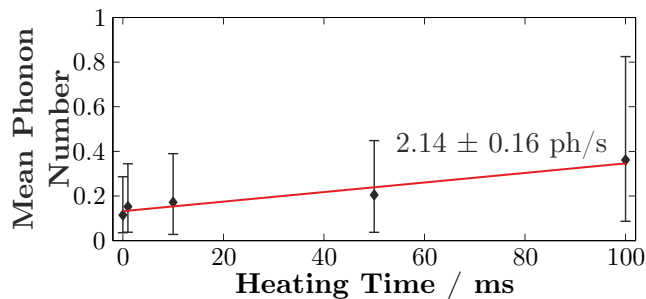


FIG. 17. Axial heating rate measurement for a trap with an ion-electrode distance of $113 \mu\text{m}$ and a secular motion frequency of 1.1 MHz .

cooling and idling for different wait times, as shown in Fig. 17. The measured heating rate for the axial mode of vibration of a single ion is $2.14(16)$ phonons/s, which is similar to results of other experiments with an electrode-ion distance close to our distance of $113 \mu\text{m}$ and a secular motion frequency close to 1.1 MHz in cryogenic setups⁸. From this, we conclude that the slot in the center of the trap does not affect the heating rate.

Another important quantity to characterize the performance of an apparatus for quantum information processing is the coherence time. In a Ramsey experiments, we prepare a balanced superposition of the two qubit states. After a wait time, one tries to rotate the state back into one of the two qubit states. By varying the phase of the second operation, one obtains a sine-like dependence of the excitation probability over the varied phase. The contrast of this sine contains information on the amount of noise present during the wait time. Hence, the Ramsey contrast in dependence of the wait time is a measure of coherence of the system.

The Ramsey measurement on the $|S, m_j = -1/2\rangle$ to $|D, m_j = -1/2\rangle$ transition, shown in Figure 18, resulted in a Gaussian decay of the Ramsey contrast with a $1/e$ -

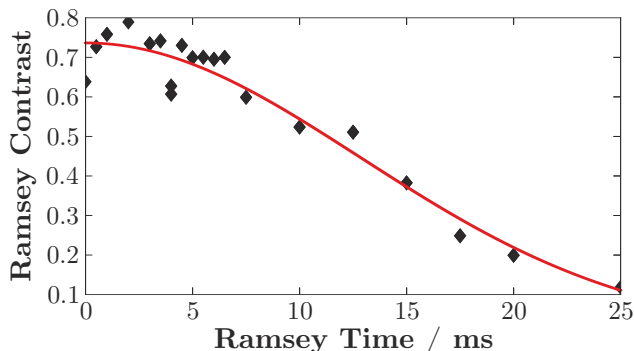


FIG. 18. Ramsey experiment with an optical $^{40}\text{Ca}^+$ qubit on the $|S, m_j = -1/2\rangle$ to $|D, m_j = -1/2\rangle$ transition in our setup, during which the optical table did not float, resulted in a Gaussian decay with a $1/e$ -time of $18.2(8) \text{ ms}$.

time of $18.2(8) \text{ ms}$. While the observed coherence time is sufficient for performing quantum gate operations, still, from the measured magnetic shielding efficiency of the inner heat shield, we would expect that the qubit phase coherence is ultimately limited by the qubit state lifetime. In future, we plan to float the optical table on its air-damped platform to minimize the dependence of the coherence of an optical qubit on acoustic vibrations.

VI. CONCLUSION

In this work, we presented our new cryogenic ion trap experiment containing observation and addressing optics, and RF enhancement resonator inside inner heat shield. A detailed study of the mechanical vibrations was shown which yielded vibrations on the order to 1 % of the qubit laser wavelength. Furthermore, a frequency analysis of the shielding against magnetic field noise in the lab was performed resulting in an upper bound of -120 dB of the reduction of 50 Hz magnetic signals along the quantization axis.

In addition to our cryostat, we described the laser setup required for the operation with $^{40}\text{Ca}^+$ and $^{88}\text{Sr}^+$ ions. The qubit laser for $^{40}\text{Ca}^+$ could be characterized with a second narrow laser at the same frequency. We observed a beat frequency of $1.58(2) \text{ Hz}$ between the two lasers and a lowest Allan deviation of $2.4 \cdot 10^{-15}$ at a time interval of 0.33 s .

Furthermore, we presented our new electronic setup, which allowed us to perform first measurements with ions. The detection and addressing optics were characterized. Moreover, Rabi flops, heating rates, and coherence times were measured. Because of the low vibrations, the high magnetic shielding, suitable laser and electronics setup, we believe this work provides an experimental platform suitable for a fault-tolerant trapped ion quantum computer.

ACKNOWLEDGMENTS

This research was funded by the Office of the Director of National Intelligence (ODNI), Intelligence Advanced Research Projects Activity (IARPA), through the Army Research Office grants W911NF-10-1-0284 and W911NF-16-1-0070. All statements of fact, opinion or conclusions contained herein are those of the authors and should not be construed as representing the official views or policies of IARPA, the ODNI, or the U.S. Government. Financial support was provided by the Austrian Science Foundation (FWF), through the SFB FoQuS (FWF project F4002-N16) as well as the Institut für Quantenoptik und Quanteninformation GmbH. P.S. was supported by the FWF Erwin Schrödinger Stipendium 3600-N27.

¹W. Paul, Review of Modern Physics **62**, 531 (1990).

²M. Chwalla, J. Benhelm, K. Kim, G. Kirchmair, T. Monz, M. Riebe, P. Schindler, A. S. Villar, W. Hänsel, C. F. Roos,

- R. Blatt, M. Abgrall, G. Santarelli, G. D. Rovera, , and P. Laurent, *Physical Review Letters* **102** (2009).
- ³H. S. Margolis, G. Huang, G. P. Barwood, S. N. Lea, H. A. Klein, W. R. C. Rowley, and P. Gill, *Physical Review A* **67** (2003).
- ⁴D. Porras and J. I. Cirac, *Phys. Rev. Lett.* **92**, 207901 (2004).
- ⁵D. Kielpinski, C. Monroe, and D. J. Wineland, *Nature* **417**, 709 (2002).
- ⁶J. Kim and C. Kim, *Quantum Info. Comput.* **9**, 181 (2009).
- ⁷S. Seidelin, J. Chiaverini, R. Reichle, J. J. Bollinger, D. Leibfried, J. Britton, J. H. Wesenberg, R. B. Blakestad, R. J. Epstein, D. B. Hume, W. M. Itano, J. D. Jost, C. Langer, R. Ozeri, N. Shiga, and D. J. Wineland, *Phys. Rev. Lett.* **96**, 253003 (2006).
- ⁸M. Brownnutt, M. Kumph, P. Rabl, and R. Blatt, *Rev. Mod. Phys.* **87**, 1419 (2015).
- ⁹J. Labaziewicz, Y. Ge, P. Antohi, D. Leibbrandt, K. R. Brown, and I. L. Chuang, *Physical Review Letters* **100** (2008).
- ¹⁰J. Chiaverini and J. M. Sage, *Physical Review A* **89** (2014).
- ¹¹P. Richerme, Z. X. Gong, A. Lee, C. Senko, J. Smith, M. Foss-Feig, S. Michalakis, A. V. Gorshkov, and C. Monroe, *Nature* **511**, 198 (2014).
- ¹²P. Jurcevic, B. Lanyon, P. Hauke, C. Hempel, P. Zoller, R. Blatt, and C. Roos, *Nature* **511**, 202 (2014).
- ¹³M. Diederich, H. Häffner, N. Hermanspahn, M. Immel, H. Kluge, R. Ley, R. Mann, W. Quint, S. Stahl, and G. Werth, *Hyperfine Interactions* **115**, 185 (1998).
- ¹⁴P. Schindler, D. Nigg, T. Monz, J. T. Barreiro, E. Martinez, S. X. Wang, S. Quint, M. F. Brandl, V. Nebendahl, C. F. Roos, M. Chwalla, M. Hennrich, and R. Blatt, *New Journal of Physics* **15**, 123012 (2013).
- ¹⁵K. R. Brown, A. C. Wilson, Y. Colombe, C. Ospelkaus, A. M. Meier, E. Knill, D. Leibfried, and D. J. Wineland, *Physical Review A* **84** (2011).
- ¹⁶A. Walther, F. Ziesel, T. Ruster, S. T. Dawkins, K. Ott, M. Hettrich, K. Singer, F. Schmidt-Kaler, and U. Poschinger, *Physical Review Letters* **109** (2012).
- ¹⁷D. J. Larson, J. C. Bergquist, J. J. Bollinger, W. M. Itano, and D. J. Wineland, *Phys. Rev. Lett.* **57**, 70 (1986).
- ¹⁸D. Kielpinski, B. E. King, C. J. Myatt, C. A. Sackett, Q. A. Turchette, W. M. Itano, C. Monroe, D. J. Wineland, and W. H. Zurek, *Phys. Rev. A* **61**, 032310 (2000).
- ¹⁹R. Ozeri, *Contemporary Physics* **52**, 531 (2011), <http://dx.doi.org/10.1080/00107514.2011.603578>.
- ²⁰*Janis* Model ST-400-1.
- ²¹The actual vibrations can be significantly larger depending on how the cryogenic system is mounted.
- ²²T. Tomaru, T. Suzuki, T. Haruyama, T. Shintomi, N. Sato, A. Yamamoto, Y. Ikushima, R. Li, T. Akutsu, T. Uchiyama, and S. Miyoki, in *Cyrocoolers* (Springer US, 2005) pp. 695–702.
- ²³T. Monz, P. Schindler, J. T. Barreiro, M. Chwalla, D. Nigg, W. A. Coish, M. Harlander, W. Hänsel, M. Hennrich, and R. Blatt, *Phys. Rev. Lett.* **106**, 130506 (2011).
- ²⁴D. Nigg, M. Müller, E. Martinez, P. Schindler, M. Hennrich, T. Monz, M. A. Martin-Delgado, and R. Blatt, *Science* **345**, 302 (2014).
- ²⁵T. Monz, D. Nigg, E. A. Martinez, M. F. Brandl, P. Schindler, R. Rines, S. X. Wang, I. L. Chuang, and R. Blatt, *Science* **351**, 1068 (2016).
- ²⁶G. Tommaseo, T. Pfeil, G. Revalde, G. Werth, P. Indelicato, and J. Desclaux, *The European Physical Journal D* **25**, 113 (2003).
- ²⁷G. P. Barwood, G. Huang, S. A. King, H. A. Klein, and P. Gill, *Journal of Physics B: Atomic, Molecular and Optical Physics* **48** (2015).
- ²⁸M. Chwalla, *Precision spectroscopy with $^{40}\text{Ca}^+$ ions in a Paul trap*, Ph.D. thesis, Universität Innsbruck (2009).
- ²⁹*Honeywell* HMC1001 and HMC1002.
- ³⁰L. Viola and S. Lloyd, *Phys. Rev. A* **58**, 2733 (1998).
- ³¹A. Barenco, C. H. Bennett, R. Cleve, D. P. DiVincenzo, N. Margolus, P. Shor, T. Sleator, J. Smolin, and H. Weinfurter, *Physical Review A* **52**, 3457 (1995).
- ³²H. C. Nägerl, D. Leibfried, H. Rohde, G. Thalhammer, J. Eschner, F. Schmidt-Kaler, and R. Blatt, *Phys. Rev. A* **60**, 145 (1999).
- ³³D. F. V. James, *Appl. Phys. B* **66**, 181 (1998).
- ³⁴Translume Inc., 655 Phoenix Dr, Ann Arbor, MI 48108, United States.
- ³⁵In total, we used four different angles for evaporation to prevent electric connection through the trenches, while making sure that the side walls as well as the center slit are coated. Under each angle we first deposited 10 nm of titanium for adhesion and then 300 nm of gold.
- ³⁶*Thorlabs* AL-1225.
- ³⁷Andor iXon+ EMCCD-Detector, 512 × 512 pixel, 16 μm.
- ³⁸M. F. Brandl, P. Schindler, T. Monz, and R. Blatt, “Cryogenic resonator design for trapped ion experiments in paul traps,” (2016), arXiv:1601.06699.
- ³⁹*Alvatec*, Gewerbestraße 3, 9112 Griffen, Austria.
- ⁴⁰S. Gulde, D. Rotter, P. Barton, F. Schmidt-Kaler, R. Blatt, and W. Hogervorst, *Applied Physics B* **73**, 861 (2001).
- ⁴¹M. Brownnutt, V. Letchumanan, G. Wilpers, R. C. Thompson, P. Gill, and A. G. Sinclair, *Applied Physics B* **87**, 411 (2007).
- ⁴²*Toptica* DL Pro from Toptica Photonics AG, Lochhamer Schlag 19, 82166 Gräfelfing, Germany.
- ⁴³*Toptica* DL pro.
- ⁴⁴R. W. P. Drever, J. L. Hall, F. V. Kowalski, J. Hough, G. M. Ford, A. J. Munley, and H. Ward, *Applied Physics B* **31**, 97 (1983).
- ⁴⁵*Toptica* TA SHG pro.
- ⁴⁶*Toptica* TA pro.
- ⁴⁷A. D. Ludlow, X. Huang, M. Notcutt, T. Zanon-Willette, S. M. Foreman, M. M. Boyd, S. Blatt, and J. Ye, *Optics Letters* **32**, 641 (2007).
- ⁴⁸*Stable Laser Systems*, 4946 63rd Street, Suite B, Boulder, CO 80301, USA.
- ⁴⁹L. Postler, *Ein schmalbandiges Halbleiter-Lasersystem für Quanteninformationsverarbeitung und Spektroskopie*, Master’s thesis, Universität Innsbruck (2015).
- ⁵⁰F. Schreck, “Control system,” (2015), <http://www.strontiumbec.com/> visited on 02.03.2016.
- ⁵¹*SAES Getters*, Viale Italia, 77, 20020 Lainate MI, Italy.
- ⁵²J. Cirac and P. Zoller, *Physical Review Letters* **74** (1995).
- ⁵³A. Sørensen and K. Mølmer, *Physical Review A* **62** (2000).